Journal of Sol-Gel Science and Technology (2025) 115:1580–1597
https://doi.org/10.1007/s10971-025-06872-9

ORIGINAL PAPER

Novel bio-inspired fabrication of $BiVO_4$ nanoparticles and their solar light-aided photocatalytic activity for metronidazole antibiotic degradation

Yogita Abhale[1] · Kajalben Patel[1] · Ruhit Kumar Paul[2] · Soumya Ranjan Mishra[2] · Saptarshi Roy[2] · Md. Ahmaruzzaman[2] · Tan Kar Ban[3] · Deepak Kumar[4] · Suresh Ghotekar[5]

Received: 21 February 2025 / Accepted: 4 July 2025 / Published online: 19 July 2025

Abstract

A popular natural sweetener with a long history of ethnomedical uses dating back to ancient civilizations, honey is a viscous liquid with an amber tint noted for its abundance of bioactive components. This investigation used a honey solution containing bioactive phytoconstituents to create bismuth vanadate nanoparticles ($BiVO_4$ NPs) for the first time. XRD, UV-Vis, FTIR, TEM, SAED pattern, SEM, EDX mapping, XPS, EIS, and BET studies highlighted the physicochemical features of as-prepared $BiVO_4$ NPs. XRD verified the biogenic synthesis of NPs, demonstrating a monoclinic scheelite structure with single-phase purity in the produced material. FTIR peaks at 1315 cm^{-1} and 1148 cm^{-1} indicate protein structures in the green source-mediated $BiVO_4$ NPs. Biosynthesized $BiVO_4$ NPs exhibit a quasi-spherical morphology with a median particle size of 25.74 nm. Moreover, the photocatalytic efficacy was disclosed by assessing the degradation rate of metronidazole, and various parameters influencing catalytic performance were investigated to attain maximum degradation efficiency. In a mere forty minutes, honey-mediated $BiVO_4$ NPs demonstrated substantial degradation of the metronidazole drug under solar light, accomplished an optimal degradation of 71.04% under the reaction conditions of 0.4 mL H_2O_2, 0.5 g/L catalyst, and 10 mg/L metronidazole concentration. Furthermore, the scavenging test was used to identify the radicals implicated in metronidazole degradation in the presence of a $BiVO_4$ photocatalyst. This study indicates that $BiVO_4$ NPs have significant potential for ecological restoration using photocatalysis.

✉ Yogita Abhale
mahayogi.85@gmail.com

✉ Suresh Ghotekar
ghotekarsuresh7@gmail.com

[1] Department of Chemistry, Government College Daman (Veer Narmad South Gujarat University, Surat), Daman 396210 DNH & DD, India

[2] Department of Chemistry, National Institute of Technology Silchar, Assam 788010, India

[3] Department of Chemistry, Universiti Putra Malaysia, 43400 UPM Serdang, Selangor, Malaysia

[4] Department of Chemistry, Manipal University Jaipur, Jaipur, Rajasthan 303007, India

[5] Department of Chemistry, Smt. Devkiba Mohansinhji Chauhan College of Commerce & Science (University of Mumbai), DNH & DD, Silvassa 396230, India

Graphical Abstract

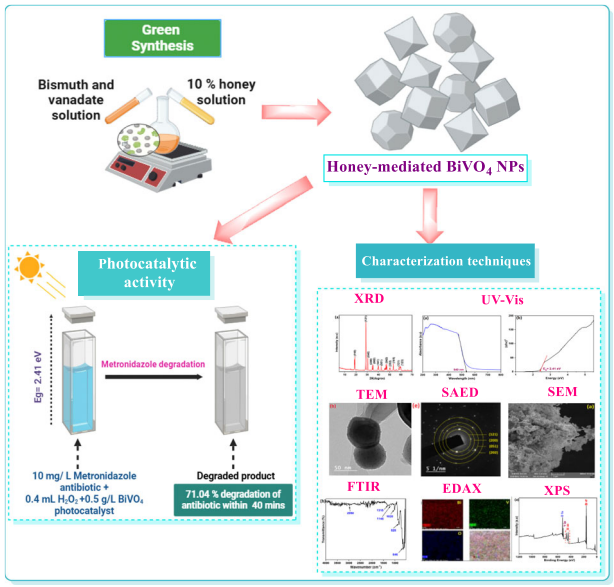

Keywords Bismuth vanadate nanoparticles · green synthesis · honey · metronidazole · photocatalysis

Highlights

- Bismuth vanadate nanoparticles ($BiVO_4$ NPs) were fabricated via a facile and bio-inspired approach.
- The physicochemical traits of $BiVO_4$ NPs were analyzed using distinctive characterization methods.
- The solar light-assisted photocatalysis study was assessed to determine the degradation of metronidazole antibiotics under diverse reaction parameters.
- Photocatalytic studies disclosed 71.44% degradation of MTZ within 40 min.

1 Introduction

Pharmaceuticals and personal care products (PPCPs) have recently been identified as emanating environmental pollutants, with several being categorized as "priority pollutants" by both the regulatory bodies of the US Environmental Protection Agency and the European Union Water Framework Directive [1]. Certain PPCPs pose ecological risks, such as developing antimicrobial resistance and disrupting the endocrine system [2–4]. Among these, antibiotics, widely employed in veterinary and human medicine, as food supplements, and as growth promoters in husbandries, have been extensively studied. Since the 1950s, the widespread usage of diverse pharmaceutical compounds—driven by population growth and advances in medical science—has led to detecting these substances in groundwater, surface water, and wastewater effluents. One such compound, metronidazole (MTZ), a commonly employed nitroimidazole derivative, is extensively administered for treating prosthesis and bacterial and protozoal infections [3, 5, 6]. In addition to its extensive use as an antibiotic for humans, MTZ is commonly employed as an additive in fish and poultry feed to combat parasites [5]. This has allowed the entrance of this compound into the aquatic ecosystem through the residuals and metabolites, resulting in long-term harms to mammalian health and the entire ecosystem [7, 8]. The residual concentrations of MTZ in aqueous environment typically range from 1-10 ng/L [9]. Owing to its high miscibility, chemical stability, and non-biodegradable characteristics, MTZ can persist and accumulate in aquatic environments [10]. Consequently, removing MTZ is a critical concern given its environmental toxicity, mutagenic potential, and carcinogenic risks damaging DNA in lymphocytes [7, 11]. Various conventional treatment approaches have been employed to address this issue, including adsorption, biological treatment methods, reduction, coagulation, flocculation, ion-exchange, and filtration. The inability of traditional water treatment systems to adequately remove antibiotics from surface and groundwater underscores the urgent need for innovative solutions to address this environmental challenge. Developing effective and cost-efficient strategies to eliminate these contaminants from the aquatic

environment completely is thus crucial for environmental protection. Advanced oxidation processes (AOPs) have emerged as an enticing approach for treating antibiotic-laden wastewater effluents, as they offer the advantage of complete mineralization of the contaminant and exhibit broad reactivity without selectivity [12]. AOPs typically involve the production of highly oxidizing $^{\bullet}OH$ intermediates, which are effective in breaking down contaminants into harmless byproducts, such as CO_2 and H_2O, via various methods such as UV/H_2O_2, UV/photocatalyst and UV/O_3 processes [10, 13]. These processes hold significant potential for efficiently degrading MTZ and other persistent contaminants in water systems. To date, heterogeneous photocatalysis technique has established their dominance as a potential strategy for the decomposition of recalcitrant and non-biodegradable contaminants with high efficiency, ease of operation, high rates of mineralization, and cost-effectiveness [14–19].

$BiVO_4$, a ternary metal oxide semiconductor with a direct band gap of roughly 2.4–2.7 eV, has manifested as an auspicious material for photocatalytic uses due to its effective function under visible light illumination, attributed to its distinctive electronic band structure and comparatively narrow band gap [20–22]. The proximity of the conduction band (CB) to the vacant Bi 6p orbitals, coupled with the overlap of anti-bonding O 2p and V 3 d states, minimizes the necessity for exterior bias to achieve efficient photocatalytic performance [21]. In addition to its photocatalytic capabilities, $BiVO_4$ exhibits a plethora of other noteworthy technological attributes, including non-toxicity, long-term photostability, good ferro elasticity, good dispersibility, and ionic conductivity. Among the three crystallographic forms of $BiVO_4$ — (i) tetragonal zircon structure (t-z), (ii) monoclinic scheelite structure (m-s), and (iii) tetragonal scheelite structure (t-s)—the thermodynamically stable monoclinic scheelite polymorph of $BiVO_4$, exhibits superior water splitting and visible-light-driven photocatalytic efficacy compared to the other phases [23–25]. Therefore, the synthesis of monoclinic $BiVO_4$ is crucial for achieving high-efficiency degradation of organic contaminants, spurring significant research into its fabrication and photocatalytic performance. Diverse physical approaches, including solvothermal, chemical vapor deposition (CVD), microwave, thermal evaporation, sputtering, pulsed laser deposition, combustion, and metal–organic CVD, have recently been explored to synthesize monoclinic $BiVO_4$ with different facet-dependent characteristics and morphologies. However, these strategies are expensive, tedious, and energy-intensive and typically require stringent experimental conditions and extended time frames. Meanwhile, multifarious wet chemistry techniques like sol-gel, solvothermal decomposition, sonochemical, electrodeposition, chemical co-precipitation, ultrasonic-assisted, hydrothermal decomposition, solution combustion, and solution plasma are more cost-effective and scalable. However, they are not always environmentally sustainable due to the implementation of noxious reducing agents and solvents [26–30]. This emphasizes the exploration and development of fabrication strategies that are both environmentally and economically friendly. To mitigate this, the concept of "green synthesis", utilizing eco-friendly reagents and biogenic processes, has gained prominence for minimizing pollution at the source and preventing waste generation [31]. One such straightforward and eco-friendly alternative is the bio-fabrication of NPs utilizing plant-based extracts, offering simplicity, cost-effectiveness, enhanced safety, and shorter duration [32–34]. These bio-extracts serve as versatile stabilizing and reducing agents, primarily attributed to the presence of various phytochemicals, including tannins, terpenoids, flavonoids, volatile oils, vitamins, and phenolic acids. They also allow improved control over the topology and size of the NPs [35].

Honey, a viscous amber-hued liquid, is an eminent natural sweetener with a rich legacy of ethno-medicinal applications tracing back to ancient civilizations [28, 29]. It has been dramatically exploited for its therapeutic potential in addressing a variety of ailments, including inflammatory conditions, cardiovascular diseases, liver disorders, cancer, and gastrointestinal issues. Contemporary research has identified a rich composition consisting of carbohydrates, vitamins, phenols, amino acids, flavonoids (such as kaempferol, quercetin, apigenin, etc.), minerals, organic acids, water, and other biomolecules as the principal beneficial bioactive components of honey [30, 31]. Some key bioactive constituents isolated are illustrated in Fig. 1. These components impart a multitude of pharmacological benefits, including antimicrobial, antioxidant, anticancer, healing of wounds, anti-diabetic, anti-aging, anti-atherosclerotic, and cardioprotective properties.

There has been limited research on the bio-fabrication of $BiVO_4$ NPs, as summarized in Table 1. Prior to this and to the best of our knowledge, no research has yet documented the bio-inspired creation of $BiVO_4$ NPs using honey as a precursor. With this perspective, the proposed study contributes, for the first time, a sustainable and bio-compatible approach for creating nanostructured $BiVO_4$, leveraging honey as a natural precursor without using any additional chemical reagents. This approach holds promise for potential applications in environmental remediation. The physicochemical characteristics of the synthesized pure-phase $BiVO_4$ were ascertained and confirmed by implementing diverse analytical techniques. Furthermore, their photocatalytic efficiency was evaluated by examining the degradation of the target contaminant, MTZ, via H_2O_2-assisted AOP under solar irradiation.

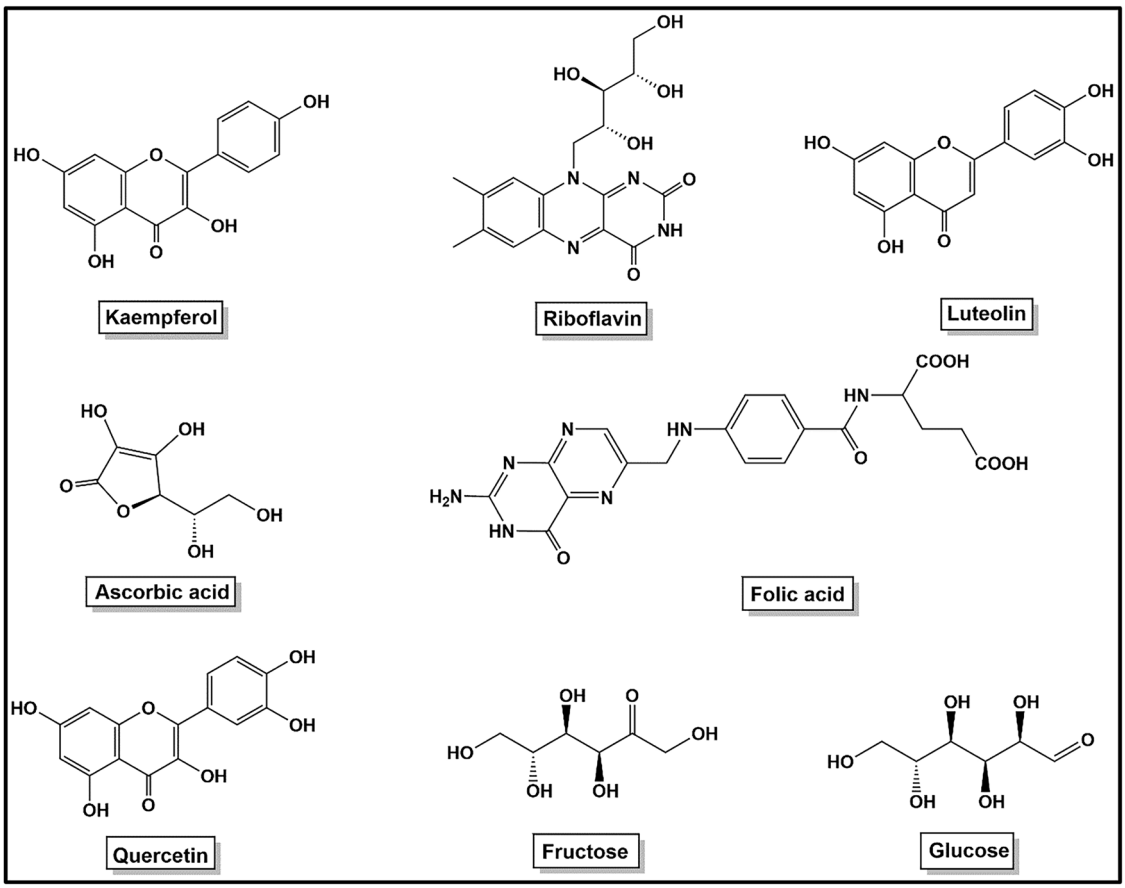

Fig. 1 Structures of some biologically essential compounds constituting honey

Table 1 Summary of previously reported biogenic fabrication of nanostructured $BiVO_4$

Plant	Specific Part	Morphology	Particle Size	Ref.
Aegle marmelos	Fruits	–	50 nm	[75]
Citrus lemon	Fruits	Irregular	75 nm	[76]
Artocarpus heterophyllus	Fruits	Quasi-spherical	32 nm	[73]
Callistemon viminalis	Flowers	Nanorods	54 nm	[77]
			7.34 nm	[20]
		Irregular disk	7.25–7.34 nm	[78]
Cow urine	—	Microspherical	38.1 nm	[31]
Hyphaene thebaica	Fruits	Nanorods	7 nm	[36]
Samanea saman	Pulp	Irregular	32 nm	[79]
Black water	—	Quasi-spherical	31 nm	[80]
Honey	—	**Quasi-spherical**	**128.1 nm**	**This work**

Bold value indicates the results of present work

2 Experimental

2.1 Materials

The analytical-grade bismuth nitrate pentahydrate ($Bi(NO_3)_3.5H_2O$) 98.5%), ammonium metavanadate (NH_4VO_3, 99%), benzoic acid ($C_7H_6O_2$), ascorbic acid, potassium persulfate ($K_2S_2O_8$), and Na_2EDTA were used in this work (purchased from SRL Chem, India). Every chemical employed in this investigation was of the highest purity and was utilized as it is. Natural honey was obtained from Nashik, India, and preserved at room temperature (RT) for later use. Distilled water (dH_2O) was employed during the experiment.

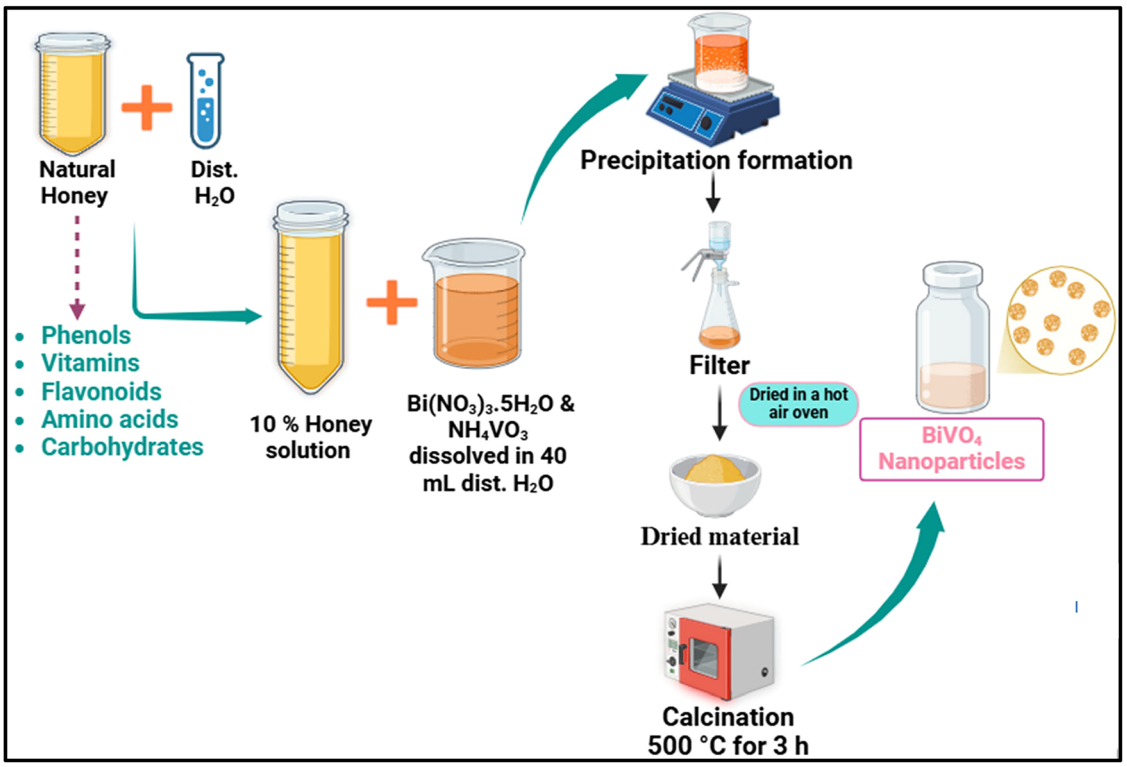

Fig. 2 Pictorial representation of honey-mediated biogenic formation of $BiVO_4$ NPs (www.biorender.com)

2.2 Bio-inspired formation of $BiVO_4$ NPs

This investigation employed bismuth nitrate, ammonium metavanadate, and phytochemical-rich natural honey as precursors to synthesize $BiVO_4$ NPs using a bio-inspired protocol. The stoichiometric ratio (1:1) of $Bi(NO_3)_3.5H_2O$ and NH_4VO_3 was poured in 40 mL of dH_2O. Then, 10 mL of honey solution was poured gradually into the mixture while swirling with a magnetic stirrer at RT for 30 min. After filtering, the precipitate was dried in an oven. Finally, the dried yellow material was annealed in a muffle furnace at 500 °C for 3 h. The yellow $BiVO_4$ NPs were crushed into a fine powder and placed for future work. Figure 2 depicts the graphical layout for the biogenic process for $BiVO_4$ NPs.

2.3 Photodegradation study

The photocatalytic efficacy of the $BiVO_4$ NPs was verified through photodegradation studies using metronidazole (MTZ) pharmaceutical (Fig. 3) as a test pollutant. The experiments were conducted under natural sunlight between 11 AM and 2 PM at the NIT Silchar campus in May. The average sunlight intensity, measured with a Lux meter, was 865 × 106 Lux, equivalent to 732.98 W/m². For the tests, 50 mL of a 10 mg/L MTZ solution was added with 0.4 g/L of the $BiVO_4$ NPs, and varying amounts of hydrogen peroxide (0–0.5 mL) were mixed to the reaction solution. The study explored different parameters, including photocatalyst dosages ranging from 0.1-0.5 g/L and MTZ concentrations between 10 and

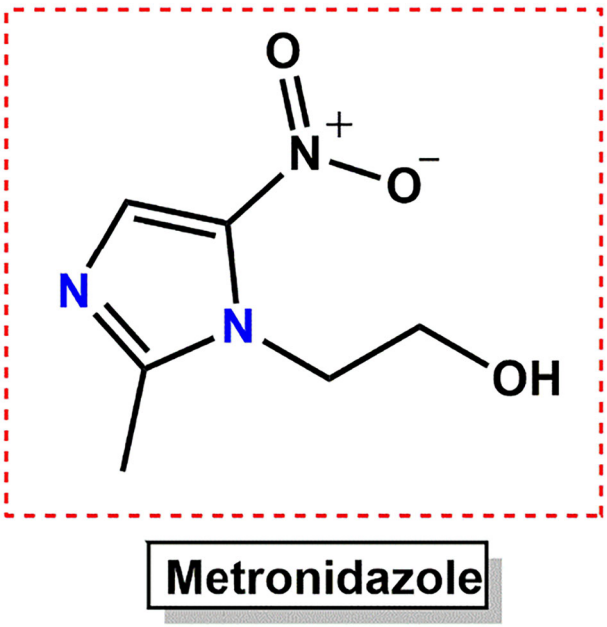

Fig. 3 Chemical structure of Metronidazole (MTZ) used in the proposed work

30 mg/L. Samples were collected at regular intervals during the experiments, centrifuged, and analyzed for changes in absorbance at 277 nm (the maximum absorption wavelength of MTZ) through a UV-visible spectrophotometer. The photodegradation efficiency (PE) of photodegradation was calculated employing the formula:

$$\mathrm{P\,E} = \frac{C_0 - C_t}{C_0} \times 100\% \quad (1)$$

2.4 Characterizations

The textural characteristics of $BiVO_4$ NPs were disclosed using distinctive characterization methods. X-ray diffraction (XRD, X'Pert-PRO PANIytical) was implemented to analyze the crystalline structure. Infrared spectra of the natural honey solution and $BiVO_4$ NPs were acquired using a Jasco 6300 FTIR spectrophotometer. Microstructural characteristics and the chemical composition of the as-prepared $BiVO_4$ NPs were disclosed with a MIRA-3 TESCAN field-emission scanning electron microscope (FESEM) equipped with an energy-dispersive X-ray (EDX) spectroscopy detector. Furthermore, a high-resolution transmission electron microscope (HRTEM, JEM-2100) was utilized to examine the morphologies of $BiVO_4$ NPs. The optical properties of the $BiVO_4$ NPs were verified using UV-Vis spectroscopy (Agilent Inc. Cary 5000) with a range of 200 to 800 nm. Utilizing XPS (XPS, PHI- VERSAPROBE III), the chemical states and composition of the biogenically produced $BiVO_4$ NPs were investigated. The surface area and porosity of the compound were revealed through a Brunauer-Emmett-Teller (BET, Quantachrome NOVA1000e, USA).

3 Results and discussion

3.1 Characterization of $BiVO_4$ NPs

3.1.1 Crystallographic structure assessment

The crystallographic characteristics of the as-produced $BiVO_4$ NPs were revealed by conducting powder XRD studies. The diffraction spectrum, illustrated in Fig. 4a, depicts distinct Bragg peaks at 18.88°, 28.91°, 30.56°, 34.59°, 35.21°, 39.88°, 42.53°, 47.26°, 50.23°, 53.25°, 58.54°, and 59.43° on the 2θ scale, corresponding to the (110), (121), (040), (200), (002), (141), (051), (042), (202), (161), (321), and (123) crystallographic reflections, respectively [36]. These peaks can be well assigned with the standard patterns, having JCPDS Card No. 01-075-1867, consistent with the earlier studies [37, 38]. The appearance of an intense peak at 28.91° and the splitting of the crystallographic peaks at 18.88°, 34.59°, and 47.26° establishes the monoclinic scheelite phase of $BiVO_4$, associated with the I2/a space group [39]. The distinct and sharp peaks reflect the highly crystalline nature of the synthesized NPs, while the absence of any additional peaks suggests the single-phase purity of the material. The Scherrer equation [40], as demonstrated in Eq. 2, was applied to estimate the average crystallite size of the $BiVO_4$ NPs to be 25.74 nm.

$$D_{hkl} = \frac{k\lambda}{\beta \cos\theta} \quad (2)$$

The FTIR data of the biosynthesized $BiVO_4$ NPs, recorded at ambient temperature, helps comprehend the bonding moieties in the synthesized NPs. Figure 4b displays a characteristic vibrational peak at 646 cm^{-1} attributable to

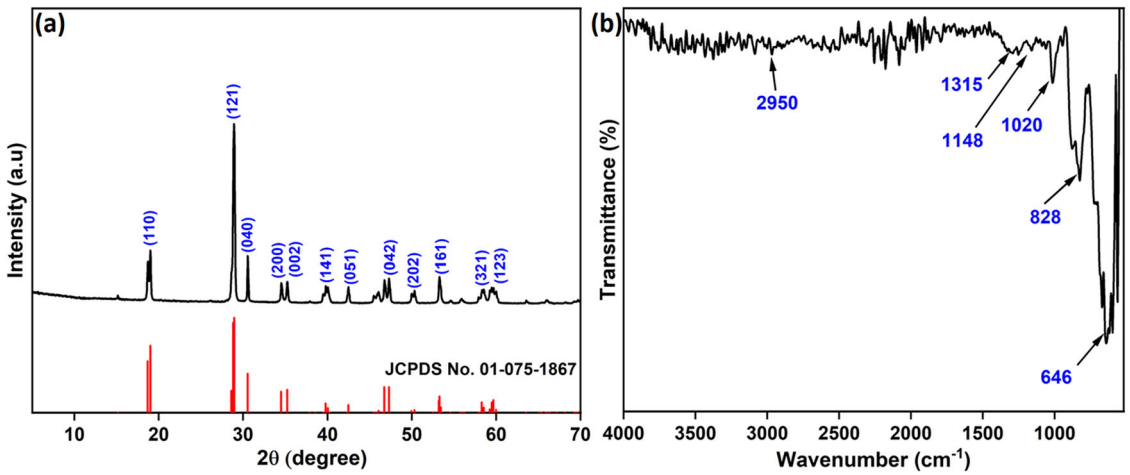

Fig. 4 **a** XRD pattern and **b** FTIR spectrum of the honey-mediated $BiVO_4$ NPs

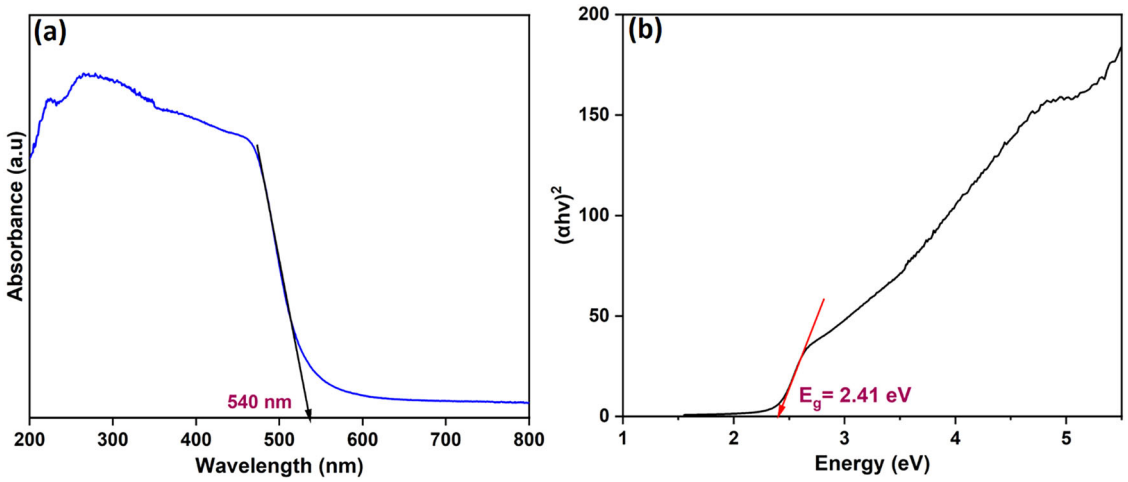

Fig. 5 **a** UV-vis spectrum and **b** band gap of the synthesized $BiVO_4$ photocatalyst determined using Tauc's plot of $(\alpha h\nu)^2$ vs. photon energy ($h\nu$)

the Bi–O bending mode [36]. The peak at 1020 cm^{-1} aligns to the unshared stretching vibrations of V = O, while the band centered at 828 cm^{-1} indicates the asymmetric stretching vibration V–O–V bond [41, 42]. Moreover, the peak at 2950 cm^{-1} is linked to the C–H stretching vibrations of carboxylic acids in low concentrations in honey. These findings are coincide with the earlier reports [43, 44]. The peaks at 1315 cm^{-1} and 1148 cm^{-1} are allocated to the C–O and C–N vibrations, reflecting the protein conformation in the honey-mediated $BiVO_4$ NPs [45, 46]. Meanwhile, the peak at 3400 cm^{-1} might be explained to the presence of residual lattice water molecules, similar to reports in earlier studies [47, 48].

3.1.2 Optical properties

The optical absorption behavior of a semiconductor, closely linked to its electronic structure, is a crucial determinant of its photocatalytic activity [49]. The synthesized sample's UV–Vis DRS is presented in Fig. 5a, exhibiting strong absorption characteristics with a sharp and steep band edge. This feature is typically attributed to the band gap transitions of semiconductors [48, 50]. Studies have reported that the valence band (VB) of $BiVO_4$ comprises of hybridized O 2p and Bi 6s orbitals, while the CB involves the V 3d orbitals. The UV absorption results from the charge-transfer transitions between the V 3d and O 2p orbitals, whereas the absorption in the visible range is ascribed to the band transitions from Bi 6s to V 3d [27]. The hybridization of Bi 6s and O 2p orbitals leads to a highly dispersed VB, which enhances the mobility of photoexcited holes and is advantageous for the photooxidation of organic contaminants. The broad absorption band observed at approximately 400-580 nm, with an absorption edge at 540 nm, suggests considerable visible light harvesting of the fabricated $BiVO_4$ sample, a crucial factor contributing to the improved photocatalytic efficiency under visible light exposure [51]. The optical band gap of a crystalline $BiVO_4$ NPs might be estimated using the equation outlined below:

$$(\alpha h\nu)^n = A\left(h\nu - E_g\right) \quad (2)$$

Here, α denotes the absorption coefficient, υ refers to the frequency of the incident photon, A refers to a constant dependent on energy, and E_g signifies the band gap of the material, respectively. The value of n relies on the nature of the electronic transition involved in the semiconductor—either a direct transition (n = 2) or an indirect transition (n = ½). The direct band gap of the produced $BiVO_4$ NPs was affirmed by plotting $(\alpha h\nu)^2$ against the photon energy ($h\nu$), as portrayed in Fig. 5b. The intercept of the tangential line at $(\alpha h\nu)^2 = 0$ provides an accurate approximation of the band gap of the as-produced photocatalyst, confirmed to be 2.41 eV. This is consistent with the previously described studies of monoclinic $BiVO_4$ structure and indicates its potential as an efficient visible-light-driven photocatalyst [27, 48, 49, 52].

3.1.3 Chemical environment analysis

Additional structural insights and determination of the elemental states constituting the as-synthesized $BiVO_4$ NPs were investigated via XPS studies. The wide scan survey spectrum in Fig. 6a confirms the presence of three elements in the sample, including bismuth, vanadium, and oxygen. The high-resolution Bi 4f spectrum in Fig. 6b might be distinctly deconvoluted into two symmetric spin-orbit components at approximately binding energies of 158.94 eV and 164.31 eV, corresponding to the Bi $4f_{7/2}$ and Bi $4f_{5/2}$, respectively [37, 49]. These signals are

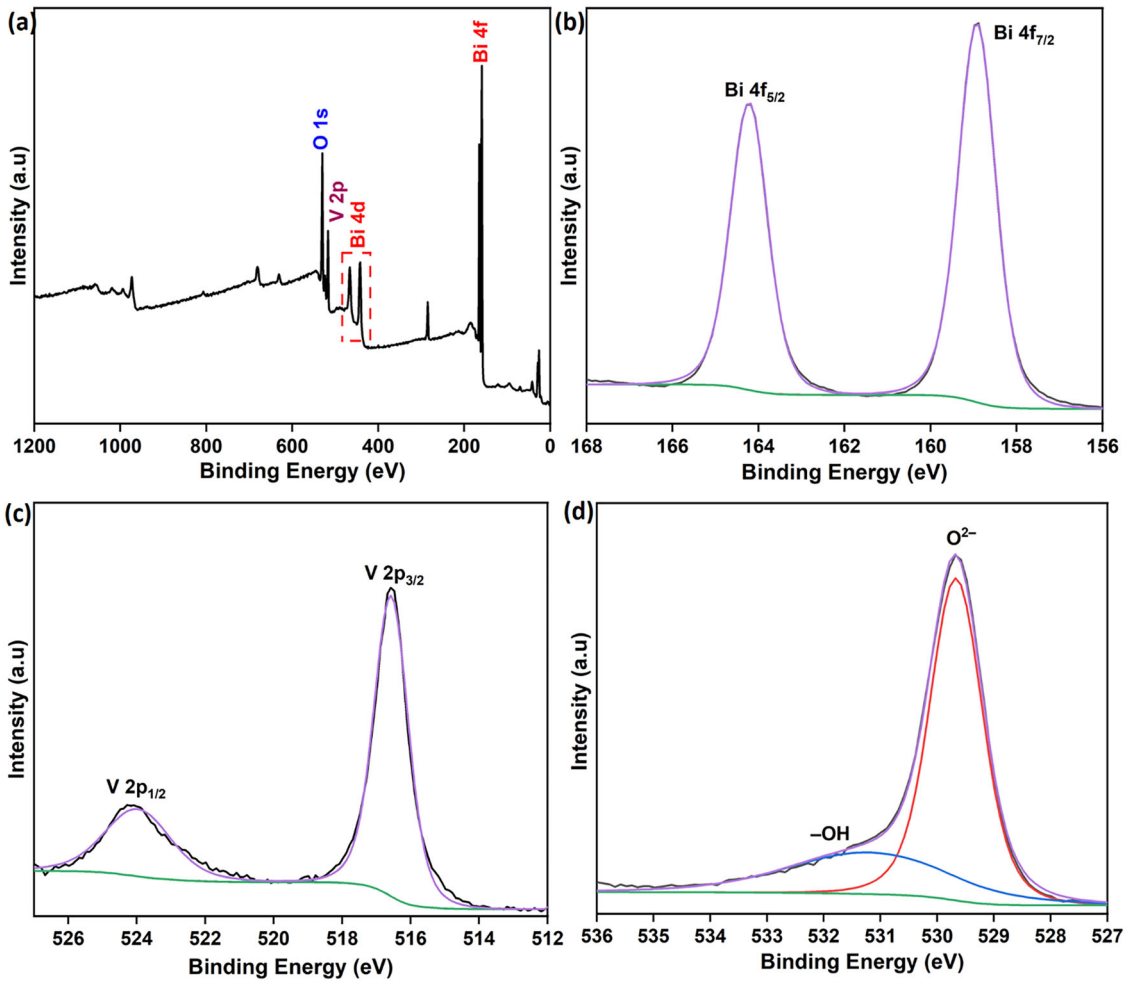

Fig. 6 **a** XPS spectrum of the as-produced $BiVO_4$ NPs, Short scan deconvoluted spectra of **b** Bi 4f, **c** V 2p, and **d** O 1s

characteristics of Bi^{3+} in the synthesized sample [53]. Similarly, the two distinct peaks in the short scan V 2p HR-XPS at binding energy values of 516.57 eV and 523.95 eV might be assigned to the V $2p_{3/2}$ and V $2p_{1/2}$ states, assignable to the surface V^{5+} species (Fig. 6c) [49, 54–57]. Moreover, the short scan O 1s spectrum, depicted in Fig. 6d, portrays an asymmetric narrow peak, suggesting the presence of multiple surface oxygen species. Deconvolution of this peak reveals subpeaks at binding energy positions of 529.68 eV and 531.15 eV, which can be associated with the lattice O^{2-} ions in crystalline $BiVO_4$ and the surface chemisorbed oxygen, respectively [37, 49, 58].

3.1.4 SEM and TEM study

The morphological features and microstructure of the as-produced NPs were obtained by SEM imaging. Figure 7a, b present both the low- and high-resolution of the SEM micrographs. Upon closer inspection, the crystal morphology was revealed to form a quasi-spherical structure with noticeable agglomeration (Fig. 7b). The particles are relatively dense, with a mean size of approximately 200 nm (Fig. 7c, d). Elemental analysis was confirmed via EDAX analysis, depicting Bi, V, and O as the prominent major elements marked in Fig. 7e. Additionally, the homogeneous distribution of the elements on the surface of $BiVO_4$ nanostructures was elucidated from the elemental mapping, as illustrated in Fig. 7f.

The micromorphology, size distribution, and crystallinity of the fabricated nanocrystalline $BiVO_4$ particles were further visualized using TEM and SAED analysis, with the results presented in Fig. 8. The TEM micrographs illustrated in Fig. 8a, b reveals that the $BiVO_4$ NPs consists of nearly spherical shaped particles in the nanoscale range with well-defined edges, aligning with the SEM observations. The interplanar spacing, calculated from the distinct lattice fringes in the HR-TEM images (Fig. 8c, d) using ImageJ software, was ascertained to be 0.31 nm, which corresponds well with the (121) crystal facet of $BiVO_4$, in agreement with the XRD results [59, 60]. The particle size distribution curve estimates the mean size of the particle to be 128.1 nm according to the statistical analysis (Fig. 8e). The bright

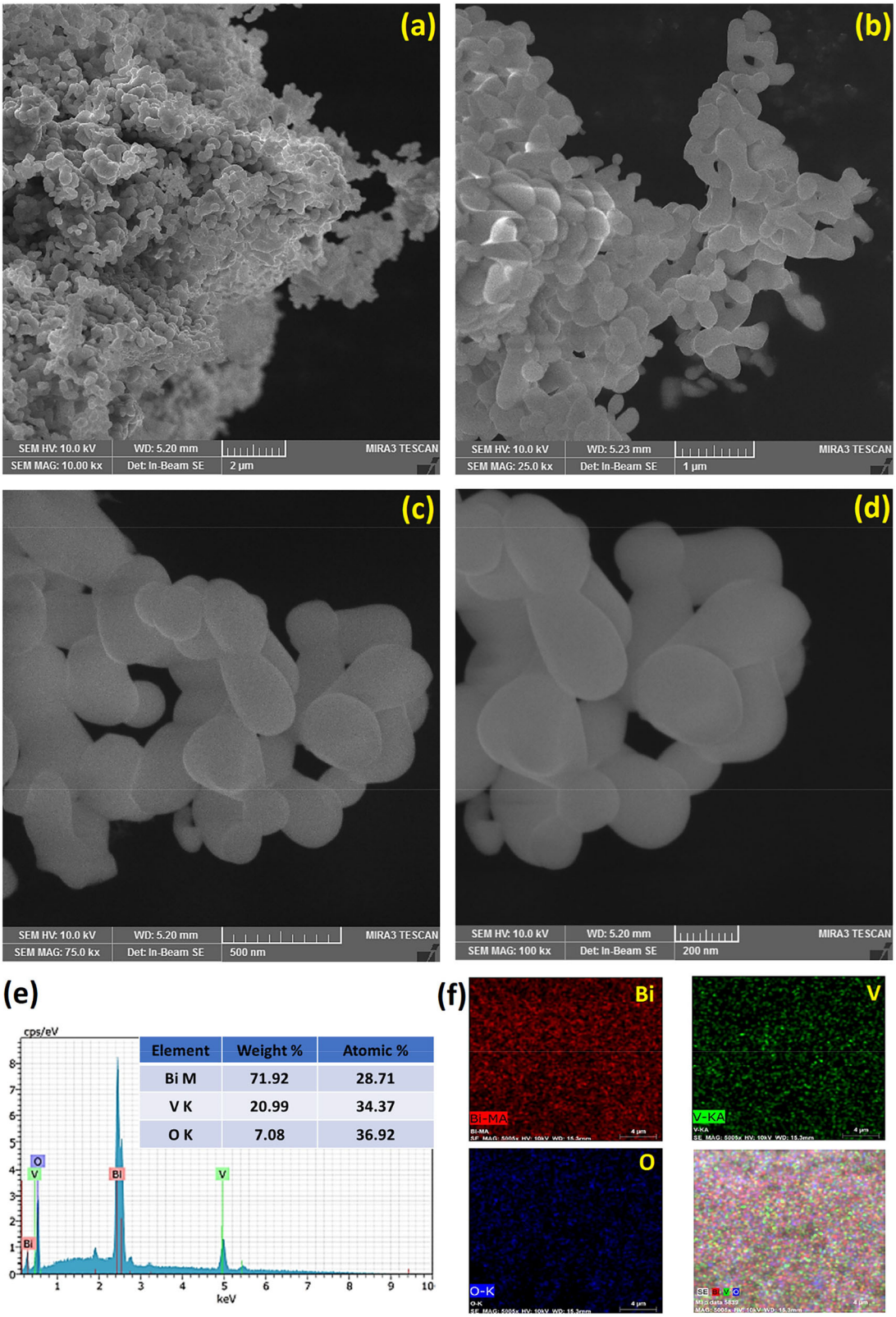

Fig. 7 **a**–**d** SEM micrographs of the as-manufactured $BiVO_4$ NPs recorded at distinct magnifications, **e** EDS spectrum, and **f** Mapping images showing the uniform distribution of the compositional elements

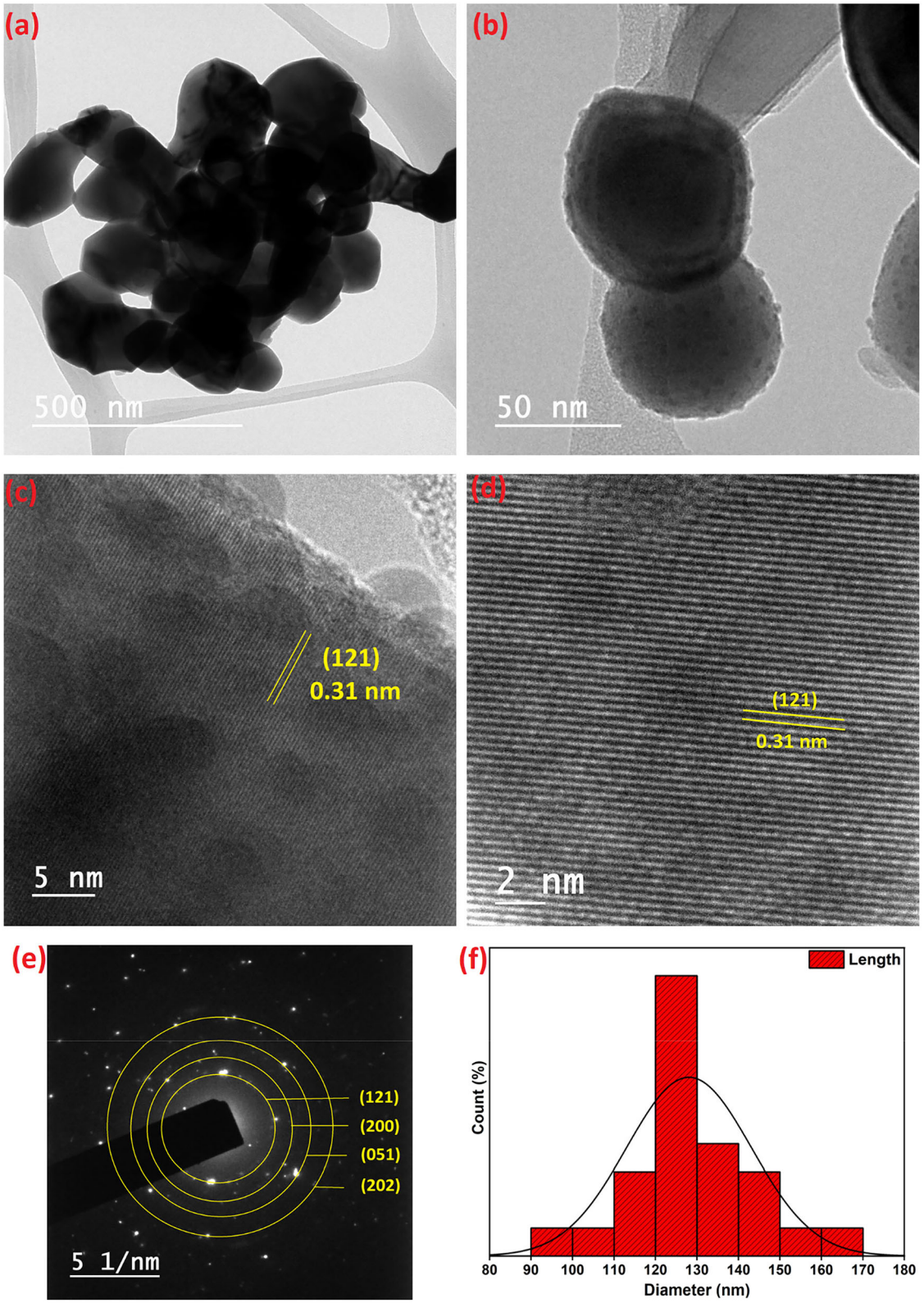

Fig. 8 **a** TEM and **b** HR-TEM micrographs of the synthesized $BiVO_4$ nanostructures at different resolutions, **c**, **d** HR-TEM image highlighting (121) crystal facet with an interplanar spacing of 0.31 nm, **e** electron diffraction patterns correlating with the XRD patterns, and **f** particle size distribution curve

diffraction spots noticed in the SAED patterns suggest the crystalline nature of the manufactured sample. The concentric rings correspond to the (121), (200), (051), and (202) crystal planes, which are identified using the standard JCPDS File and match the XRD results presented above (Fig. 8f) [61–63]. Therefore, the combined XRD and TEM analyses disclose the effective development of $BiVO_4$, with no impurities or secondary crystalline phases detected.

3.1.5 Surface area analysis

Comprehensive insights into the fabricated nanostructured material's porosity and surface properties can be performed using the BET analysis. The correlation between the relative pressure (P/P_0) and the adsorbed volume, as presented in Fig. 9, unveils the particular type of isotherm and the hysteresis loop involved. In line with IUPAC guidelines, the displayed N_2 adsorption-desorption isotherm indicates an ideal Type IV curve, confirming the porous structure of the material [8, 64]. Additionally, the results reveal a hysteresis loop approaching near $P/P_0 = 1$, a characteristic feature of Type IV isotherms, indicating the meso-porosity of the nanomaterial. The structure and presence of this hysteresis loop offer a crucial understanding of the pore structure of the photocatalyst. The noticeable increase in the volume adsorbed at higher relative pressures, coupled with the distinct separation of the adsorption and desorption branches, points to an H1 hysteresis loop, characteristic of uniform mesopores. The $BiVO_4$ NPs exhibited a specific surface area of 11.38 m²/g and a mesopore volume of 0.036 cm³/g, indicating the existence of mesopores with a calculated pore diameter of 2.161 nm, as depicted in the pore size distribution (PSD) pattern (inset of Fig. 9). Notably, the BET-surface area of the synthesized $BiVO_4$ NPs is considerably larger than previously reported values for $BiVO_4$ hollow microspheres (1.05 m²/g) [65], $BiVO_4$ hierarchical microtubes (0.3 m^2/g) [66], porous $BiVO_4$ (5.69 m^2/g) [67], and $BiVO_4$ hollow spheres (5.85 m²/g) [68]. This increased specific surface area enhances the photocatalytic ability of the material. The mesopore volume also creates active catalytic sites for contaminant interaction, further improving the photocatalytic performance. However, the overall photocatalytic efficiency is influenced by the surface area and other vital factors, such as reduced band gap and optimal porosity, which are critical in determining the photocatalytic activity [13].

3.2 The impacts of reaction conditions on photocatalytic study

3.2.1 Impact of H_2O_2

Hydrogen peroxide (H_2O_2) is a prominent oxidizing agent and a crucial component in advanced oxidation processes (AOP) for photodegradation of organic molecules. Metronidazole (MTZ) photodegradation was investigated at different H_2O_2 doses, ranging from 0 to 0.5 mL per 50 mL of a 10 mg/L pharmaceutical solution, with a constant $BiVO_4$ NPs (photocatalyst) dosage of 0.4 g/L. As shown in Fig. 10, MTZ decomposition efficacy was 35.93% without H_2O_2. This efficiency improved significantly to 60.97% at a 0.4 mL/50 mL dose but dropped afterward. Increasing the H_2O_2 dose increases hydroxyl radicals ($OH^{\bullet}$) production from H_2O_2 breakdown. However, an unfavorable effect on the decomposition rate was observed at higher H_2O_2 concentrations due to the quenching reaction taking place at higher $OH^{\bullet}$ concentrations producing less reactive $HO_2^{\bullet}$ radicals based

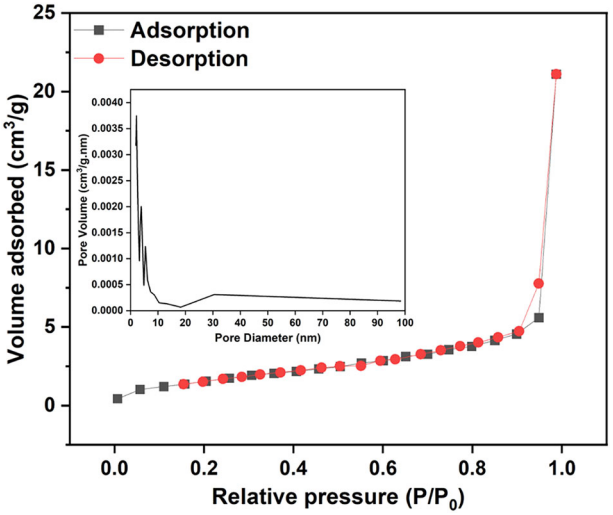

Fig. 9 N_2 adsorption-desorption isotherm and the PSD curve (inset) of the fabricated $BiVO_4$ NPs

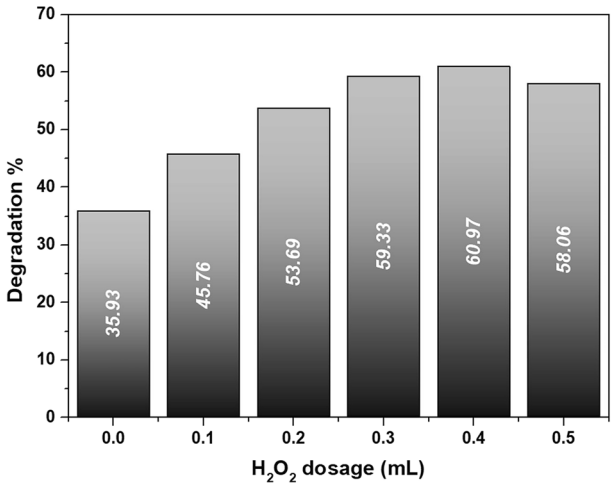

Fig. 10 Impact of H_2O_2 dosage on MTZ degradation

on the reaction as follows:

$$H_2O_2 \overset{BiVO_4}{\rightarrow} 2OH^{\bullet}$$

$$H_2O_2 + OH^{\bullet} \rightarrow H_2O + HO_2^{\bullet}$$

3.2.2 Effect of catalyst dosage

The influence of photocatalyst ($BiVO_4$ NPs) loading on MTZ decomposition was revealed by varying the concentration from 0.4 to 0.8 g/L in a 10 mg/L MTZ solution with a constant H_2O_2 dose of 0.4 mL. As depicted in Fig. 11, MTZ degradation capacity initially improved with increasing photocatalyst concentrations due to improved surface active sites for pollutant interaction and increased creation of reactive oxygen species (ROS). The highest decomposition rate of 71.04% was attained with an optimum photocatalyst loading of 0.5 g/L. However, additional increases in photocatalyst concentration led to decreased degradation efficiency. This drop is due to the excessive dispersion of $BiVO_4$ particles, which raises the turbidity of the solution and impedes photon penetration. Furthermore, an excess photocatalyst can produce excess hydroxyl radicals ($OH^{\bullet}$), which can recombine, lowering MTZ degradation efficiency. As a result, an appropriate $BiVO_4$ NPs loading of 0.5 g/L was identified for this method.

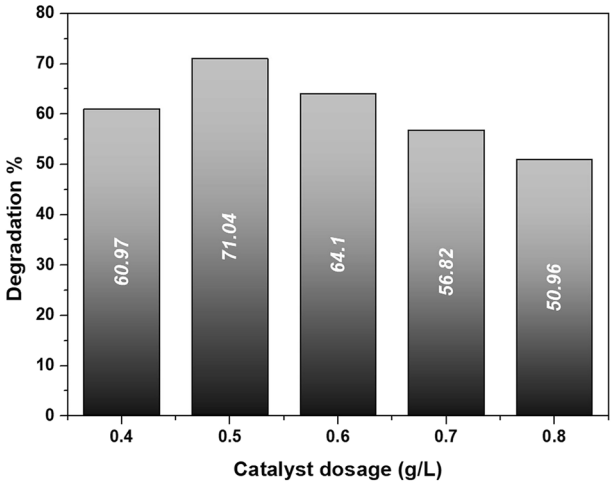

Fig. 11 Impact of $BiVO_4$ dosage on MTZ degradation

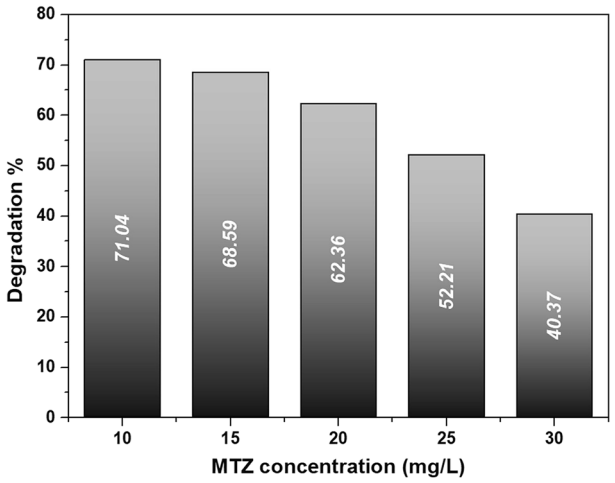

Fig. 12 Impact of MTZ concentration on MTZ degradation

3.2.3 Impact of MTZ concentration

The ideal concentration of MTZ was determined by adjusting the concentration from 10 to 30 mg/L while maintaining appropriate H_2O_2 dose and photocatalyst loading. Figure 12 shows that an MTZ concentration of 10 mg/L resulted in the highest degradation performance of 71.04%. Beyond this concentration, deterioration efficiency decreased. The concentration of MTZ increases the opacity of the solution, preventing light penetration to the photocatalyst surface. Furthermore, larger concentrations of MTZ require a more considerable amount of ROS for successful degradation, which necessitates a higher photocatalyst loading, lowering photodegradation efficiency. Furthermore, increased MTZ molecules might block the photocatalyst's surface sites, reducing ROS generation and overall degrading capacity. As a result, a dye concentration of 10 mg/L was shown to be the most effective for degradation efficiency.

3.2.4 Kinetic studies

The optimal degradation was 71.04%, with a reaction condition of 0.4 mL H_2O_2, 0.5 g/L $BiVO_4$ NPs, 10 mg/L of MTZ concentration with 40 min of visible light irradiation. The kinetics of the photodecomposition of MTZ was depending on the pseudo-first-order (PFO) kinetic model based on the below equation:

$$\ln \frac{C_0}{C} = kt \tag{3}$$

Here, k is the rate constant, and C_0 and C are the starting and final MTZ concentrations under ideal parameters at time t.

The kinetics of MTZ antibiotic photodegradation is represented in Fig. 13. MTZ degradation demonstrated a PFO rate constant of 0.03047 min^{-1}.

3.2.5 Reusability analysis

Reusability is an essential quality for commercializing photocatalysts. The reusability of the produced $BiVO_4$ photocatalyst was tested over several cycles. After each cycle, the photocatalyst was collected, washed several times with methanol to renew its active sites, and dried at 100 °C for three hours before reuse. As seen in Fig. 14, the $BiVO_4$ photocatalyst sustained photocatalytic activity for up to four cycles without significantly decreasing efficiency. However, further cycles revealed a significant decline in deterioration efficiency. This decrease in photocatalytic capacity is linked to the degradation of active sites on the $BiVO_4$ caused by repeated regeneration and reuse operations. Despite this, the photocatalyst achieved a noteworthy reusability efficiency of 50.98% in the fourth cycle, demonstrating that $BiVO_4$ is stable and resistant to photocorrosion. A comparative investigation of the XRD patterns of the fabricated $BiVO_4$ photocatalyst prior to (Fig. 4a) and after the photodegradation process (Fig. 15) reveals no noticeable change in diffraction peaks designated to the crystallographic planes of $BiVO_4$ in the reused sample. This observation confirms that $BiVO_4$ does not leach during the photocatalytic reaction and has considerable stability.

3.2.6 Scavengers analysis

The production of ROS and charge carriers has a substantial impact on dye degradation. A scavenging study was executed to determine the significant radicals involved in metronidazole (MTZ) degradation in the presence of a $BiVO_4$ photocatalyst (Fig. 16). This test employed 0.1 mmol of benzoic acid as a hydroxyl scavenger, ascorbic

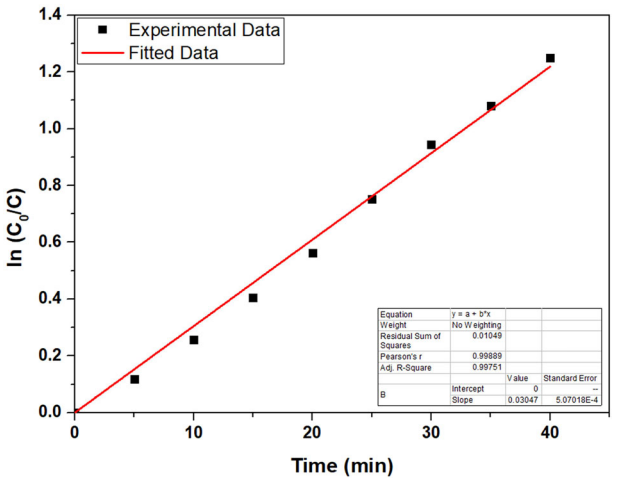

Fig. 13 MTZ degradation kinetics for determination of reaction rate

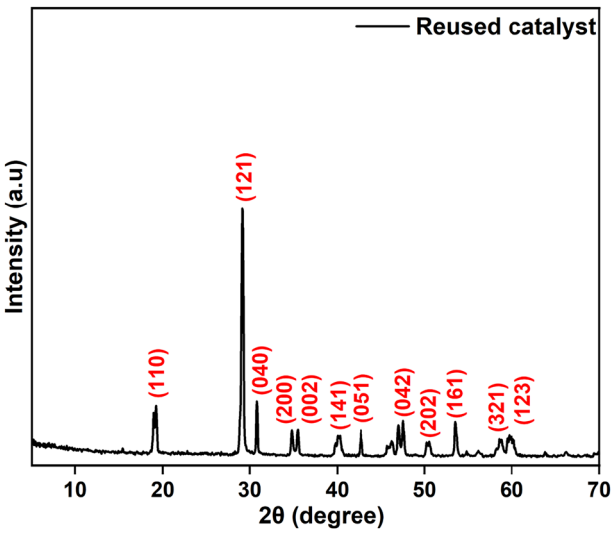

Fig. 15 XRD analysis of reused $BiVO_4$ nanocatalyst after MTZ degradation

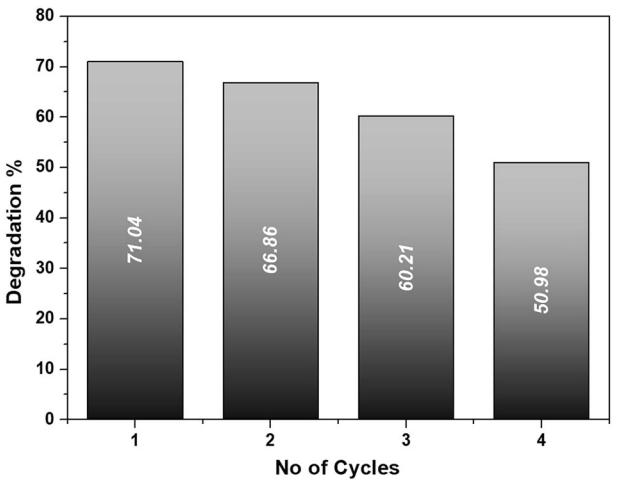

Fig. 14 Reusability study of $BiVO_4$ nanocatalyst for MTZ degradation

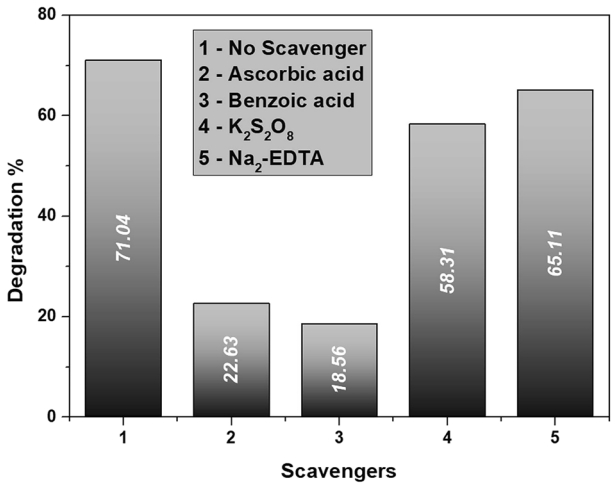

Fig. 16 Impact of diverse scavengers on decomposition of MTZ

acid as a superoxide scavenger, disodium EDTA (Na_2EDTA) as a hole scavenger, and $K_2S_2O_8$ as an electron scavenger. The findings showed that including AA and BA substantially lowered degrading capacity to 22.63% and 18.56%, respectively. This indicates that hydroxyl and superoxide radicals are essential in the photodegradation of MTZ antibiotics. In contrast, the functions of electrons and holes were discovered to be minimal in this process.

3.3 Photocatalytic mechanism

A tenable photocatalytic mechanism has been put up to explain the photocatalytic efficacy of $BiVO_4$ nanoparticles in sunlight after taking into account the aforementioned results (Fig. 17). When light with the right energy reached the surface of $BiVO_4$ nanoparticles, photoexcited electrons and hole pairs were produced in the CB and VB, respectively, achieving the photocatalytic destruction of MTZ [69]. To create active species, the as-formed electrons participate in redox processes. From previous studies the VB position of the $BiVO_4$ nanoparticles was found to be 2.72 eV, using Mulliken's formula [31]. The bandgap of the fabricated nanomaterial was computed to be 2.41 eV employing the Tauc's plot and the CB position was estimated to be 0.31 eV. The potential necessary for ROS formation is crucial, as water molecules or hydroxide ions (OH^-) must be oxidized to create $^{\bullet}OH$ radicals ($^{\bullet}OH/H_2O = +1.99$ eV/NHE, $^{\bullet}OH/OH^- = +2.40$ eV/NHE). The VB location of $BiVO_4$ (2.72 eV) is sufficiently positive to permit this oxidation reaction. To further boost ROS formation, H_2O_2 was introduced during the reaction. H_2O_2 serves as an electron acceptor and decomposes into $^{\bullet}OH$ and $O_2^{\bullet-}$ radicals under visible light, increasing reactive species' availability. However, the CB is not sufficiently negative to reduce oxygen molecules into $O_2^{\bullet-}$ radicals, the presence of surface defects and oxygen vacancies might facilitate electron mitigation leading to O_2 reduction, as can be confirmed via scavenger analysis [70].

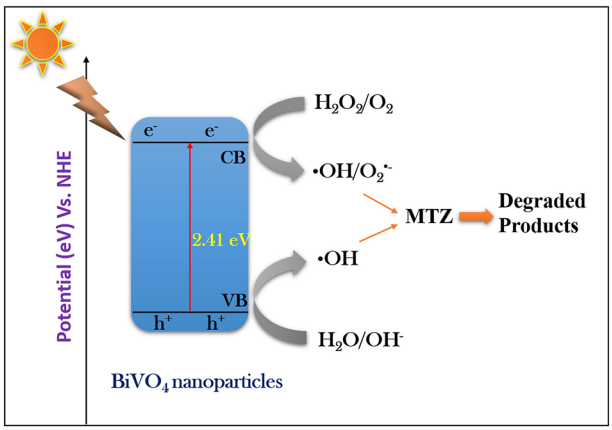

Fig. 17 Plausible photocatalytic mechanism for the degradation of metronidazole via $BiVO_4$ nanoparticles

3.4 Comparison of MTZ degradation using diverse catalyst

Due to its balanced performance and environmentally benign preparation, the green-synthesized $BiVO_4$ photocatalyst shows great promise, as indicated in Table 2. With a solid elimination capability of 21.3 mg/g.h, it degrades MTZ by more than 71.04% in just 40 min, outperforming several other compounds that require larger doses or longer timeframes. It offers a more straightforward, environmentally friendly, and scalable water treatment option compared to intricate nanocomposites. It is, therefore, a viable option for environmentally friendly treatment.

3.5 Electrochemical impedance spectroscopy (EIS) study

The electrode $BiVO_4$, synthesized using green techniques, was analyzed using EIS to assess both the interfacial charge transport and the resistance attributes. In the Nyquist plot (Fig. 18), there is a distinctive semicircular arc at the high-to-mid frequency region, with a linear segment at lower

Table 2 The comparison of the photocatalytic performance of $BiVO_4$ NPs with reported catalysts for MTZ degradation

Photocatalyst	Catalyst dosage (g/L)	MTZ conc. (mg/L)	Rate (min^{-1})	Time (min)	Efficiency (%)	Removal capacity (mg/g.h)	Ref.
Modified CuO NPs	2	50	0.0624	60	98.36	24.59	[81]
Modified TiO_2 NPs	0.5	80	0.0513	180	99.48	53.23	[15]
$Ce_2Sn_2O_7$–Sb_2O_3/biochar	0.4	20	—	80	95	35.71	[82]
$Zn_{0.75}Ni_{0.25}Fe_2O_4$	0.8	5	—	70	92.9	4.97	[83]
TiO_2/$CuBi_2O_4$@graphene oxide	1	10	0.0312	120	97.86	4.89	[84]
Greenly synthesized $BiVO_4$	**0.5**	**10**	**0.03047**	**40**	**71.04**	**21.3**	**This work**

Bold value indicates the results of present work

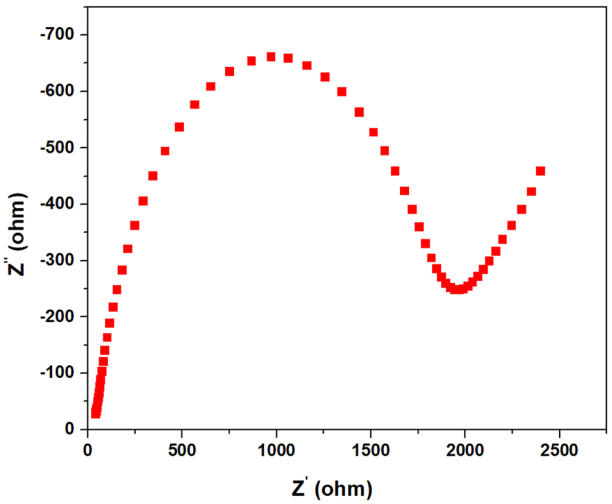

Fig. 18 EIS graph of greenly synthesized $BiVO_4$ nanoparticles

frequencies that is less steep. The semicircle shows R_{ct}, or charge-transfer resistance, found at the interface electrode-electrolyte. The electrolytic conductivity intercepted as R_s. For the equivalent circuit, R_s was estimated to be about 1965 Ω, and R_{ct} was approximately 665 Ω. The electrolyte is believed to cause moderate ohmic resistance, which, along with the relatively high resistance, suggests R_{ct} is due to the $BiVO_4$/electrolyte interface. The semicircular shape also suggests non-ideal capacitive behavior that is caused by the surface rupture and porous shape of the $BiVO_4$ material. The high Z' slopes relate to the confirmation of ion transport limitations toward the electrode structure. Overall, the EIS results suggest that the green-synthesized $BiVO_4$ exhibits moderate charge-transfer characteristics.

The lower R_{ct} seen here suggests improved interfacial charge transfer as opposed to pure $BiVO_4$, which usually shows a much higher R_{ct} because of its innately low electrical conductivity and constrained charge mobility [71, 72]. The inclusion of stabilizing phytochemicals or bio-reducing agents added during green synthesis may have contributed to this enhancement by enhancing surface area, improving crystallinity, or creating advantageous surface states that aid in charge transfer [73]. The existence of a Warburg-type diffusion tail and a lower R_{ct} indicate that the green-synthesized $BiVO_4$ provides quicker interfacial kinetics and more effective ionic diffusion than its chemically synthesized equivalent [74]. These findings demonstrate how green synthesis techniques may be used to produce $BiVO_4$-based materials with enhanced electrochemical characteristics for use in photocatalysis.

4 Conclusion

Through a biogenic process, $BiVO_4$ NPs were created for the first time in this work employing natural honey assigned as a reducing/stabilizing agent. The textural features of honey-mediated $BiVO_4$ NPs were analyzed using XRD, UV-Vis, FTIR, TEM, SAED pattern, SEM, EDX mapping, XPS, EIS, and BET studies. The prepared $BiVO_4$ NPs, according to EDAX spectra, are primarily composed of Bi, V, and O. SEM imaging shows that they possess a quasi-spherical morphology. XPS study affirmed the presence of Bi^{+3}, V^{+5}, and O^{-2} and provided data on the atomic composition of the $BiVO_4$ NPs, which was consistent with the results obtained from FTIR and EDX. Considering its potential for successful photocatalytic applications, the as-prepared $BiVO_4$ photocatalyst's band gap was confirmed to be 2.41 eV. The photocatalytic efficacy of $BiVO_4$ NPs for the decomposition of the MTZ antibiotic was assessed under sunlight, resulting in a degradation rate of 71.04% within 40 min. This process followed a PFO kinetic model with a rate constant of 0.03047 min^{-1}. Because more ROS are produced and there are more active sites, the efficiency of MTZ breakdown increases with increasing photocatalyst concentration. The reusability test disclosed that the photocatalyst had a considerable reusability efficiency of 50.98% in the fourth cycle. The scavenging experiment indicated that hydroxyl and superoxide radicals are necessary for MTZ photodegradation. The biogenic process of synthesizing NPs using honey is a straightforward, cost-effective, non-toxic, and eco-friendly method that demonstrates significant photocatalytic efficiency.

Data availability

Data will be made available on request.

Acknowledgements This work is financially supported by the Sajjan India Limited (now, Cohizon Life Sciences Limited)-supported Center of Excellence on Green Technologies for Sustainable Development, Dharmsinh Desai University, Nadiad (Gujarat), India. We also acknowledge the NIT Silchar and MARC Bengaluru, for supplying the characterization services.

Author contributions Yogita Abhale: Supervision, Writing- Original draft preparation. Kajalben Patel, Ruhit Kumar Pal, and Deepak Kumar: Writing- Original draft preparation. Soumya Ranjan Mishra and Saptarshi Roy: Formal analysis, Methodology, Writing- Original draft preparation Md. Ahmaruzzaman and Tan Kar Ban: Writing – review & editing. Suresh Ghotekar: Investigation, Methodology, Supervision, Writing – review & editing.

Compliance with ethical standards

Conflict of interest The authors declare no competing interests.

References

1. Murray KE, Thomas SM, Bodour AA (2010) Prioritizing research for trace pollutants and emerging contaminants in the freshwater environment. Environ Pollut 158(12):3462–3471

2. Yang X et al. (2011) Occurrence and removal of pharmaceuticals and personal care products (PPCPs) in an advanced wastewater reclamation plant. Water Res 45(16):5218–5228
3. Dong S et al. (2014) Facile synthesis of novel ZnO/RGO hybrid nanocomposites with enhanced catalytic performance for visible-light-driven photodegradation of metronidazole. Mater Chem Phys 145(3):357–365
4. Manoharan RK et al. (2020) Antibacterial and photocatalytic activities of 5-nitroindole capped bimetal nanoparticles against multidrug resistant bacteria. Colloids Surf B: Biointerfaces 188:110825
5. Farzadkia M et al. (2014) Degradation of metronidazole in aqueous solution by nano-ZnO/UV photocatalytic process. Desalination Water Treat 52(25-27):4947–4952
6. Shah NB et al. (2015) Anaerobic prosthetic joint infection. Anaerobe 36:1–8
7. Malakootian M et al. (2019) Photocatalytic degradation of metronidazole from aquatic solution by TiO 2-doped Fe 3+ nano-photocatalyst. Int J Environ Sci Technol 16:4275–4284
8. Roy S et al. (2024) Anchoring Ni (II) bisacetylacetonate complex into CuS immobilized MOF for enhanced removal of tinidazole and metronidazole. npj Clean Water 7(1):83
9. Wagil M et al. (2015) Determination of metronidazole residues in water, sediment and fish tissue samples. Chemosphere 119:S28–S34
10. Hao R et al. (2012) Efficient adsorption and visible-light photocatalytic degradation of tetracycline hydrochloride using mesoporous BiOI microspheres. J Hazard Mater 209:137–145
11. Johnson MB, Mehrvar M (2008) Aqueous metronidazole degradation by UV/H2O2 process in single-and multi-lamp tubular photoreactors: kinetics and reactor design. Ind Eng Chem Res 47(17):6525–6537
12. Hodges BC, Cates EL, Kim J-H (2018) Challenges and prospects of advanced oxidation water treatment processes using catalytic nanomaterials. Nat nNanotechnology 13(8):642–650
13. Roy, S, et al., Harmonising light and structure: exploring ZnO/MOF composite photocatalysts for environmental remediations. International Journal of Environmental Analytical Chemistry, 2024:1-13.
14. Bashiri F et al. (2020) Enhanced photocatalytic degradation of metronidazole by TiO2 decorated on magnetic reduced graphene oxide: Characterization, optimization and reaction mechanism studies. J Mol Liq 314:113608
15. Farzadkia M et al. (2015) Photocatalytic degradation of Metronidazole with illuminated TiO 2 nanoparticles. J Environ Health Sci Eng 13:1–8
16. Asgharzadeh F et al. (2020) Heterogeneous photocatalytic degradation of metronidazole from aqueous solutions using Fe3O4/TiO2 supported on biochar. Desalination Water Treat 175:304–315
17. Dubey, V, et al., Recent Advancements in Fabrication of NdVO4 Nanomaterials and Their Versatile Applications in Catalysis and Biomedical. Topics in Catalysis, 2024:1-18.
18. Nair, N, et al., Mechanisms in the photocatalytic breakdown of persistent pharmaceutical and pesticide molecules over TiO2-based photocatalysts: A review. Journal of Physics: Condensed Matter, 2024.
19. Qu Y, Duan X (2013) Progress, challenge and perspective of heterogeneous photocatalysts. Chem Soc Rev 42(7):2568–2580
20. Mohamed H et al. (2021) Biosynthesis of BiVO4 nanorods using Callistemon viminalis extracts: Photocatalytic degradation of methylene blue. Mater Today: Proc 36:328–335
21. Abraham SD et al. (2016) Eco-friendly and green synthesis of BiVO4 nanoparticle using microwave irradiation as photocatalayst for the degradation of Alizarin Red S. J Mol Struct 1113:174–181
22. Qi Y et al. (2022) Unraveling of cocatalysts photodeposited selectively on facets of BiVO4 to boost solar water splitting. Nat Commun 13(1):484
23. Zhang L, Chen D, Jiao X (2006) Monoclinic structured BiVO4 nanosheets: hydrothermal preparation, formation mechanism, and coloristic and photocatalytic properties. J Phys Chem B 110(6):2668–2673
24. Thalluri SM et al. (2016) Green-synthesized W-and Mo-doped BiVO4 oriented along the {0 4 0} facet with enhanced activity for the sun-driven water oxidation. Appl Catal B: Environ 180:630–636
25. Fan Y et al. (2021) Selective photocatalytic oxidation of methane by quantum-sized bismuth vanadate. Nat Sustainability 4(6):509–515
26. Zhou L, Wang W, Zhang L (2007) Ultrasonic-assisted synthesis of visible-light-induced Bi2MO6 (M= W, Mo) photocatalysts. J Mol Catal A: Chem 268(1-2):195–200
27. Li H, Liu G, Duan X (2009) Monoclinic BiVO4 with regular morphologies: hydrothermal synthesis, characterization and photocatalytic properties. Mater Chem Phys 115(1):9–13
28. Jiang H et al. (2012) Hydrothermal fabrication and visible-light-driven photocatalytic properties of bismuth vanadate with multiple morphologies and/or porous structures for Methyl Orange degradation. J Environ Sci 24(3):449–457
29. Wang M, Liu Q, Luan HY (2011) Preparation, characterization and photocatalytic preoperty of BiVO4 photocatalyst by sol-gel method. Appl Mech Mater 99:1307–1311
30. Dunkle SS, Helmich RJ, Suslick KS (2009) BiVO4 as a visible-light photocatalyst prepared by ultrasonic spray pyrolysis. J Phys Chem C 113(28):11980–11983
31. Ghotekar S et al. (2024) A novel eco-benevolent synthesis of BiVO4 nanoparticles using cow urine for antioxidant, anticancer, and photocatalytic activities. Biomass- Convers Biorefinery 14(23):29613–29629
32. Cuong HN et al. (2022) New frontiers in the plant extract mediated biosynthesis of copper oxide (CuO) nanoparticles and their potential applications: A review. Environ Res 203:111858
33. Patel, K, et al., Unveiling new frontiers in advancements of bio-inspired fabrication of cadmium-based nanomaterials for biomedical and catalytic applications–A review. Inorganic Chemistry Communications, 2024:113457.
34. Patel, K, et al., A critical review on Lantana camara extract-mediated bio-inspired synthesis of nanomaterials and their potential application: Challenges and future perspectives. Inorganic Chemistry Communications, 2025:113830.
35. Q. Alijani H, Iravani S, Varma RS (2022) Bismuth vanadate (BiVO4) nanostructures: eco-friendly synthesis and their photocatalytic applications. Catalysts 13(1):59
36. Mohamed HEA et al. (2019) Phytosynthesis of BiVO 4 nanorods using Hyphaene thebaica for diverse biomedical applications. AMB Express 9:1–14
37. Nguyen VH et al. (2019) Effective photocatalytic activity of sulfate-modified BiVO4 for the decomposition of methylene blue under LED visible light. Materials 12(17):2681
38. Pham MQ et al. (2020) Facile solvothermal synthesis of highly active monoclinic scheelite BiVO4 for photocatalytic degradation of methylene blue under white LED light irradiation. Arab J Chem 13(11):8388–8394
39. Khan I et al. (2017) Sonochemical assisted hydrothermal synthesis of pseudo-flower shaped Bismuth vanadate (BiVO4) and their solar-driven water splitting application. Ultrason Sonochem 36:386–392
40. Holzwarth U, Gibson N (2011) The Scherrer equation versus the'Debye-Scherrer equation'. Nat Nanotechnol 6(9):534–534

41. Zulkifili AN, Fujiki A, Kimijima S (2018) Flower-like BiVO4 microspheres and their visible light-driven photocatalytic activity. Appl Sci 8(2):216
42. Geng Y, Zhang P, Kuang S (2014) Fabrication and enhanced visible-light photocatalytic activities of BiVO 4/Bi 2 WO 6 composites. RSC Adv 4(86):46054–46059
43. Maringgal B et al. (2020) Biosynthesis of CaO nanoparticles using Trigona sp. Honey: Physicochemical characterization, antifungal activity, and cytotoxicity properties. J Mater Res Technol 9(5):11756–11768
44. Nivethitha PR, Rachel DCJ (2022) A study of antioxidant and antibacterial activity using honey mediated Chromium oxide nanoparticles and its characterization. Mater Today: Proc 48:276–281
45. Sharmila M et al. (2021) Photocatalytic and biological activity of ZnO nanoparticles using honey. Coatings 11(9):1046
46. Philip D (2009) Honey mediated green synthesis of gold nanoparticles. Spectrochimica Acta Part A: Mol Biomolecular Spectrosc 73(4):650–653
47. Liu J et al. (2003) Hydrothermal preparation of BiVO4 powders. Mater Sci Eng: B 104(1-2):36–39
48. Zhang A, Zhang J (2009) Hydrothermal processing for obtaining of BiVO4 nanoparticles. Mater Lett 63(22):1939–1942
49. Ge L (2008) Novel Pd/BiVO4 composite photocatalysts for efficient degradation of methyl orange under visible light irradiation. Mater Chem Phys 107(2-3):465–470
50. Yu J, Kudo A (2006) Effects of structural variation on the photocatalytic performance of hydrothermally synthesized BiVO4. Adv Funct Mater 16(16):2163–2169
51. Liu, Y, et al. PEG-assisted hydrothermal synthesis of novel flower-like hierarchical BiVO4 with enhanced visible light photocatalytic activity. in *IOP Conference Series: Materials Science and Engineering*. 2018. IOP Publishing.
52. Zhang X et al. (2007) Selective synthesis and visible-light photocatalytic activities of BiVO4 with different crystalline phases. Mater Chem Phys 103(1):162–167
53. Palaniselvam T et al. (2017) Vastly enhanced BiVO4 photocatalytic OER performance by NiCoO2 as cocatalyst. Adv Mater Interfaces 4(19):1700540
54. Zhang A, Zhang J (2010) Synthesis and characterization of Ag/BiVO4 composite photocatalyst. Appl Surf Sci 256(10): 3224–3227
55. Anand P et al. (2023) Morphological and elemental tuning of BiOCl/BiVO4 heterostructure for uric acid electrochemical sensor and antibiotic photocatalytic degradation. Chemosphere 310:136847
56. Zhang Q, Liu G, Liu T (2024) Oxygen evolution reaction (OER) active sites in BiVO 4 studied using density functional theory and XPS experiments. Phys Chem Chem Phys 26(3):2580–2588
57. Li J et al. (2015) Facile synthesis and high activity of novel BiVO4/FeVO4 heterojunction photocatalyst for degradation of metronidazole. Appl Surf Sci 351:270–279
58. Wang M et al. (2013) Characterization and photocatalytic properties of N-doped BiVO4 synthesized via a sol–gel method. J Alloy Compd 548:70–76
59. Zhang Q et al. (2020) Z-scheme gC 3 N 4/BiVO 4 photocatalysts with RGO as electron transport accelerator. J Mater Sci: Mater Electron 31:667–676
60. Patil SS et al. (2017) One-pot in situ hydrothermal growth of BiVO4/Ag/rGO hybrid architectures for solar water splitting and environmental remediation. Sci Rep. 7(1):8404
61. Lin H et al. (2014) One-pot hydrothermal synthesis of BiPO 4/BiVO 4 with enhanced visible-light photocatalytic activities for methylene blue degradation. RSC Adv 4(21):10968–10974
62. Bashir S et al. (2022) Gd-doped BiVO4 microstructure and its composite with a flat carbonaceous matrix to boost photocatalytic performance. J Alloy Compd 913:165214
63. Wang G-L et al. (2017) Enhanced photocatalytic properties of molybdenum-doped BiVO 4 prepared by sol–gel method. Rare Met 36:129–133
64. Roy S, Mishra SR, Ahmaruzzaman M (2024) Ultrasmall copper-metal organic framework (Cu-MOF) quantum dots decorated on waste derived biochar for enhanced removal of emerging contaminants: Synergistic effect and mechanistic insight. J Environ Manag 366:121802
65. Cheng B et al. (2012) One-pot template-free hydrothermal synthesis of monoclinic BiVO4 hollow microspheres and their enhanced visible-light photocatalytic activity. Int J Photoenergy 2012(1):797968
66. Ying Y et al. (2015) Controlled fabrication of bismuth vanadium oxide hierarchical microtubes with enhanced visible light photocatalytic activity. Mater Sci Semiconductor Process 32:82–89
67. Dong P et al. (2016) Template-free synthesis of monoclinic BiVO4 with porous structure and its high photocatalytic activity. Materials 9(8):685
68. Yin, W, et al., BiVO4 hollow nanospheres: anchoring synthesis, growth mechanism, and their application in photocatalysis. 2009, Wiley Online Library.
69. Venkatesan P et al. (2025) Enhanced solar-driven photoelectrocatalytic water treatment and hydrogen evolution with triplet-triplet annihilation upconversion with Mo-doped BiVO4 nanocomposite films. Appl Catal B: Environ Energy 365:124913
70. Sun X et al. (2019) Enhanced superoxide generation on defective surfaces for selective photooxidation. J Am Chem Soc 141(9):3797–3801
71. Rocabruno-Valdés C et al. (2024) Exploring the electronic structure of BiVO4 thin films using energy-resolved electrochemical impedance spectroscopy. Mater Lett 357:135741
72. Alshgari RA et al. (2024) Facile fabrication of bismuth vanadate grafted carbon nanotubes composite for enhanced oxygen evolution reaction. J Electroanalytical Chem 954:118025
73. Mallikarjunaswamy C et al. (2021) Green synthesis and evaluation of antiangiogenic, photocatalytic, and electrochemical activities of BiVO4 nanoparticles. J Mater Sci: Mater Electron 32(10):14028–14046
74. Hernández-Balaguera E, Vara H, Polo J (2016) An electrochemical impedance study of anomalous diffusion in PEDOT-coated carbon microfiber electrodes for neural applications. J Electroanalytical Chem 775:251–257
75. Pramila S et al. (2020) Green Synthesis of BiVO4 nanoparticles by microwave method using Aegle marmelos juice as a fuel: Photocatalytic and antimicrobial study. Anal Chem Lett 10(3):298–306
76. Manjunatha AS et al. (2018) Green synthesis of flower-like BiVO4 nanoparticles by solution combustion method using lemon (citrus limon) juice as a fuel: Photocatalytic and electrochemical study. ChemistrySelect 3(47):13456–13463
77. Mohamed, H, et al. Green synthesis of BiVO4 nanorods via aqueous extracts of Callistemon viminalis. in *AIP Conference Proceedings*. 2018. AIP Publishing.
78. Mohamed H et al. (2018) Bio-synthesis of BiVO4 nanorods using extracts of Callistemon viminalis. MRS Adv 3(42-43):2479–2486
79. Pramila S et al. (2024) Green synthesis of bismuth vanadate nanostructures for efficient photocatalytic and biological studies. Nano-Struct Nano-Objects 39:101198
80. Ghotekar S et al. (2024) A novel approach towards biosynthesis of BiVO4 nanoparticles and their anticancer, antioxidant, and photocatalytic activities. J Sol-Gel Sci Technol 109(3):784–794
81. Seid-Mohammadi A et al. (2020) Photocatalytic degradation of metronidazole (MNZ) antibiotic in aqueous media using copper oxide nanoparticles activated by H2O2/UV process: Biodegradability and kinetic studies. Desalination Water Treat 193:369–380

82. Marouani I et al. (2025) Construction of a novel coffee husk-derived biochar-supported Ce2Sn2O7-Sb2O3 composites for enhanced visible light-driven photocatalytic degradation of metronidazole and H2 production. J Water Process Eng 75:107935
83. Sharafzadeh, S, et al., Co-precipitation synthesis and characterization of Zn (II)/Ni (II) magnetic heterostructure ferrite for photocatalytic degradation of metronidazole. Surfaces and Interfaces, 2025:105917.
84. Osanloo M, Khorasheh F, Larimi A (2025) Development of a novel Z-scheme TiO2/CuBi2O4@ GO with enhanced performance for the photocatalytic degradation of metronidazole. J Water Process Eng 72:107641